Supporting Information

Catalytic electron drives host-guest recoginition

Yoshihiro Owatari, Shuta Iseki, Daiji Ogata and Junpei Yuasa*

Department of Applied Chemistry, Tokyo University of Science, 1-3 Kagurazaka, Shinjuku-ku, Tokyo 162-8601, Japan

Experimental Section

Materials and Methods: All the chemical reagents were commercially available. ^{1}H NMR spectra were measured with JNM-ECA500 (500 MHz), JEOL JNM-ECZ400S (400 MHz). UV-Vis absorption spectra were recorded by an Agilent Technologies Cary 8454 UV-visible Spectroscopy System and JASCO V-660 spectrophotometer at ambient temperature. Mass spectrum was measured with mass spectrometers (JEOL AccuTOF JMS-T100LC for ESI). All measurements were performed at room temperature. DFT studies were calculated with GAUSSIAN ’09.

Synthesis: In a two necked flask, anthraquinone (200 mg) was dissolved in acetonitrile (140 mL). Tetramethylammonium hydroxide (10% in methanol, 1.5 mL) was added dropwise to the solution and the mixture was stirred for 1 hour at room temperature. Then, acetic acid (1 mL) was added dropwise to the reaction mixture and after stirred for 10 minutes, the solution was undergone a filtration and the solvent was removed by evaporation from the filtrate. The solid residue was dissolved in $CHCl_3$ and washed by water and brine, dried by Na_2SO_4. After the solvent was removed by evaporation, the crude product was purified by silica gel column chromatography ($CHCl_3$/ethyl acetate = 3/2) to obtain white powder (90 mg, 38%). ^{1}H NMR (500 MHz, $CDCl_3$) δ 8.30 (dd, J = 8.0, 1.5 Hz, 2H), 8.07 (dd, J = 8.0, 1.5 Hz, 2H), 7.77 (td, J = 8.0, 1.5 Hz, 2H), 7.60 (td, J = 8.0, 1.5 Hz, 2H), 2.93 (s, 2H), 2.72 (s, 1H). ^{13}C NMR (100 MHz, $CDCl_3$) δ 182.52, 144.01, 134.18, 130.49, 129.50, 127.74, 125.62, 115.52 69.91, 37.85. HRMS (*m/z*) (ESI$^+$): Calculated for $C_{16}H_{11}NNaO_2^+$ $[M + Na]^+$: 272.06875, found 272.06920. The single crystal was obtained by Et_2O vapor diffusion into acetonitrile solution at room temperature. A host compound (U_HAnt_2) having anthracene tweezers was synthesized according to literature.[1]

Electrochemistry: We performed electrochemical measurements by using ALS Electrochemical Analyzer Model 1211B in deaerated acetonitrile containing 0.1 M Bu_4NClO_4 (TBAP) as the supporting electrolyte at room temperature. This study used a conventional three-electrode cell comprising of a platinum working electrode and a Pt wire as a counter electrode. The $Ag/AgNO_3$ (0.01 M) reference electrode was used to measure potentials. Thin-layer spectroscopic electrochemical experiments were performed using the optically transparent platinum thin-layer working electrode in combination with an Agilent Technologies Cary 8454 UV-visible Spectroscopy System.

ESR Measurements: AQH-CH_2CN (1.0×10^{-3} M) was dissolved in deaerated acetonitrile, then the resulting ESR tube was purged with argon for 10 min. Then, sodium naphthalene, $Np^{\bullet-}\cdot Na^+$ (0.1 M in deaerated THF) was introduced into the ESR cell containing AQH-CH_2CN (1.0×10^{-3}

M) under bubbling with an Ar gas using a long needle syringe. $Np^{\bullet-}\cdot Na^+$ was prepared according to the literature method[2,3] just before the experiments. Prior to the addition, purity of $Np^{\bullet-}\cdot Na^+$ was determined by testing performed of one-electron reduction of benzoquinone. The resulting ESR spectra of $AQ^{\bullet-}$ were recorded by BRUKER EMXnano spectrometer at 298 K.

Kinetic Measurements: AQH-CH_2CN (2.0×10^{-2} M) was dissolved in deaerated THF-d_8 and purged with argon for 10 min. Then, $Np^{\bullet-}\cdot Na^+$ (0.1 M in deaerated THF-d_8) was introduced into the NMR tube containing AQH-CH_2CN (2.0×10^{-2} M) under bubbling with an Ar gas using a long needle syringe. Purity of $Np^{\bullet-}\cdot Na^+$ was determined by testing performed of one-electron reduction of benzoquinone. Upon addition of $Np^{\bullet-}\cdot Na^+$, the colorless solution became red color immediately. The NMR spectra were recorded by JNM-ECZ400S (400 MHz) until the reaction was completed.

Thermodynamics of Reductant Upconversion (S1): DFT calculations indicate the free energies of neutral and radical-anionic versions of the fragmentation as $\Delta G_{\mathrm{rxn}} = -13.0$ kcal mol^{-1} (calc.) and $\Delta G_{\mathrm{rxn}}^{\bullet-} = -32.1$ kcal mol^{-1} (calc.), respectively. In such a case, the upconversion value ($\Delta G_{\mathrm{up}} = \Delta G_{\mathrm{rxn}}^{\bullet-} - \Delta G_{\mathrm{rxn}}$) is negative ($\Delta G_{\mathrm{up}} = -19.1$ kcal mol^{-1} (calc.)) [Fig. S1a†], and therefore no upconversion would be expected. However, the experimental data clearly show that the upconversion is real. Hence, the real $|\Delta G_{\mathrm{rxn}}^{\bullet-}|$ value should be much smaller ($|\Delta G_{\mathrm{rxn}}^{\bullet-}| < |\Delta G_{\mathrm{rxn}}|$), indicating that the real radical anionic species is more structurally and energetically close to the dissociated product (i.e., $AQ^{\bullet-} + CH_3CN$) [Fig. S1b]. It should be noted that, when we used the initial input structure with the OH hydrogen atom located close to the CH_2CN group (i.e., $(AQ\cdots H\cdot\cdot CH_2CN)^{\bullet-}$) for the DFT calculation (Fig. S2c), the dissociated product (i.e., $AQ^{\bullet-} + CH_3CN$) was obtained as the output optimized structure (Fig. S2d). Hence, unfortunately the real $\Delta G_{\mathrm{rxn}}^{\bullet-}$ value is difficult to obtain by theoretical means. Conversely, the 3.5 kcal mol^{-1} is the experimentally suggested upconversion value ($\Delta G_{\mathrm{up}} = 3.5$ kcal mol^{-1} (exp.)) [Fig. S1c].

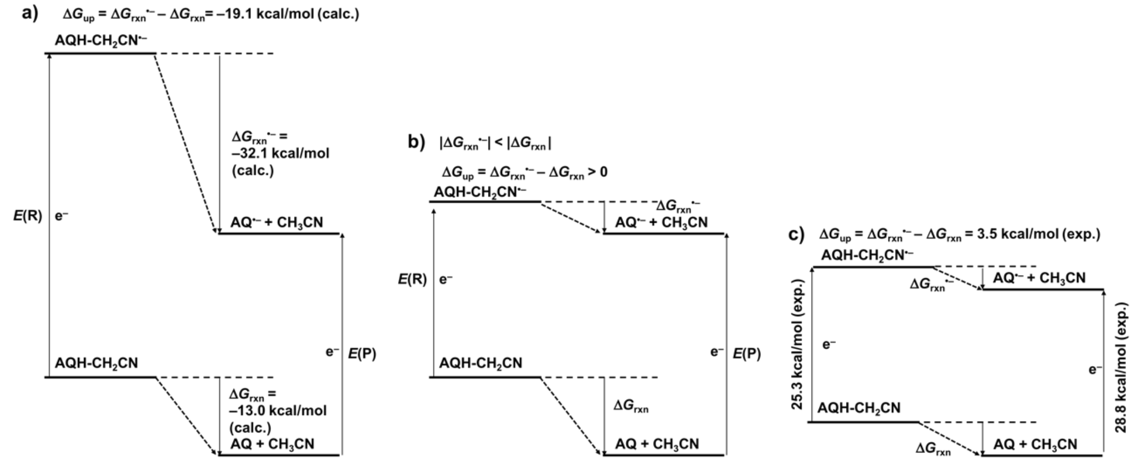

Figure S1. a) DFT-estimated thermodynamics of reductant upconversion for $AQH\text{-}CH_2CN \rightarrow AQ + CH_3CN$. b) The thermodynamics of reductant upconversion in the case that $|\Delta G_{\mathrm{rxn}}^{\bullet-}| < |\Delta G_{\mathrm{rxn}}|$, c) The experimentally suggested thermodynamics of reductant upconversion.

Fragmentation of Acetonitrile in AQH-$CH_2CN^{\bullet-}$ (S2): Although, the detailed mechanism of the fragmentation could not be established, the DFT study suggests that energy rise of AQH-$CH_2CN^{\bullet-}$ as a function of C-C distance ($d_{c\text{–}c}$) [corresponding to the C–C bond cleavage] (Fig. S2a) is much higher than those as a function of C-H distance ($d_{C\text{–}H}$) [corresponding to the intramolecular proton transfer] (Fig. S2b). Furthermore, when we used the initial input structure with the OH hydrogen atom located close to the CH_2CN group (i.e., $(AQ\cdots H\cdot\cdot CH_2CN)^{\bullet-}$) for the DFT calculation (Fig. S2c), the dissociated product (i.e., $AQ^{\bullet-}$ + CH_3CN) can be obtained as the output optimized structure (Fig. S2d). In that sense, the fragmentation is likely to be triggered by the intramolecular proton transfer.

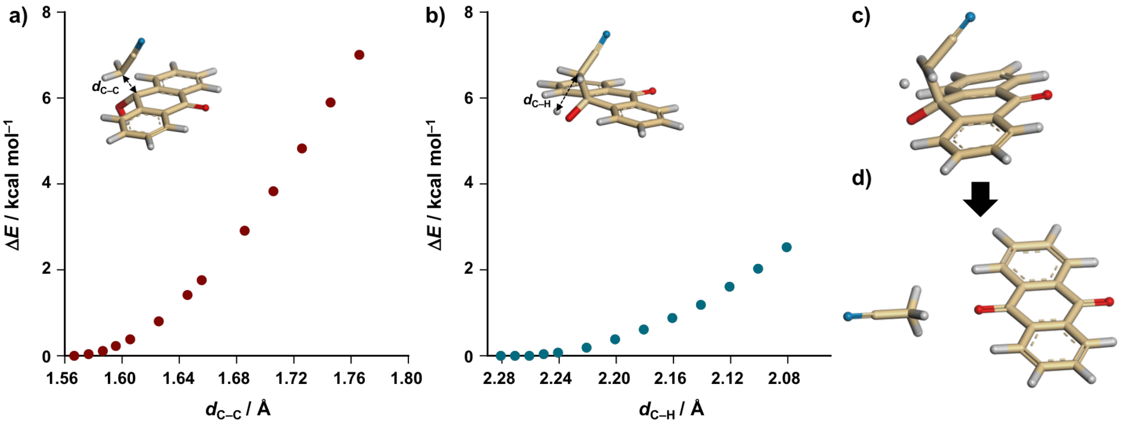

Figure S2. a,b) Changes in single point energy [DFT/UB3LYP-6-31G+(d,p)] of AQH-$CH_2CN^{\bullet-}$ as a function of a) C–C distance ($d_{C\text{–}C}$), b) C–H distance ($d_{C\text{–}H}$). c) Initial input structure of AQH-$CH_2CN^{\bullet-}$, and d) the output optimized structure [DFT/UB3LYP-6-31G+(d,p)].

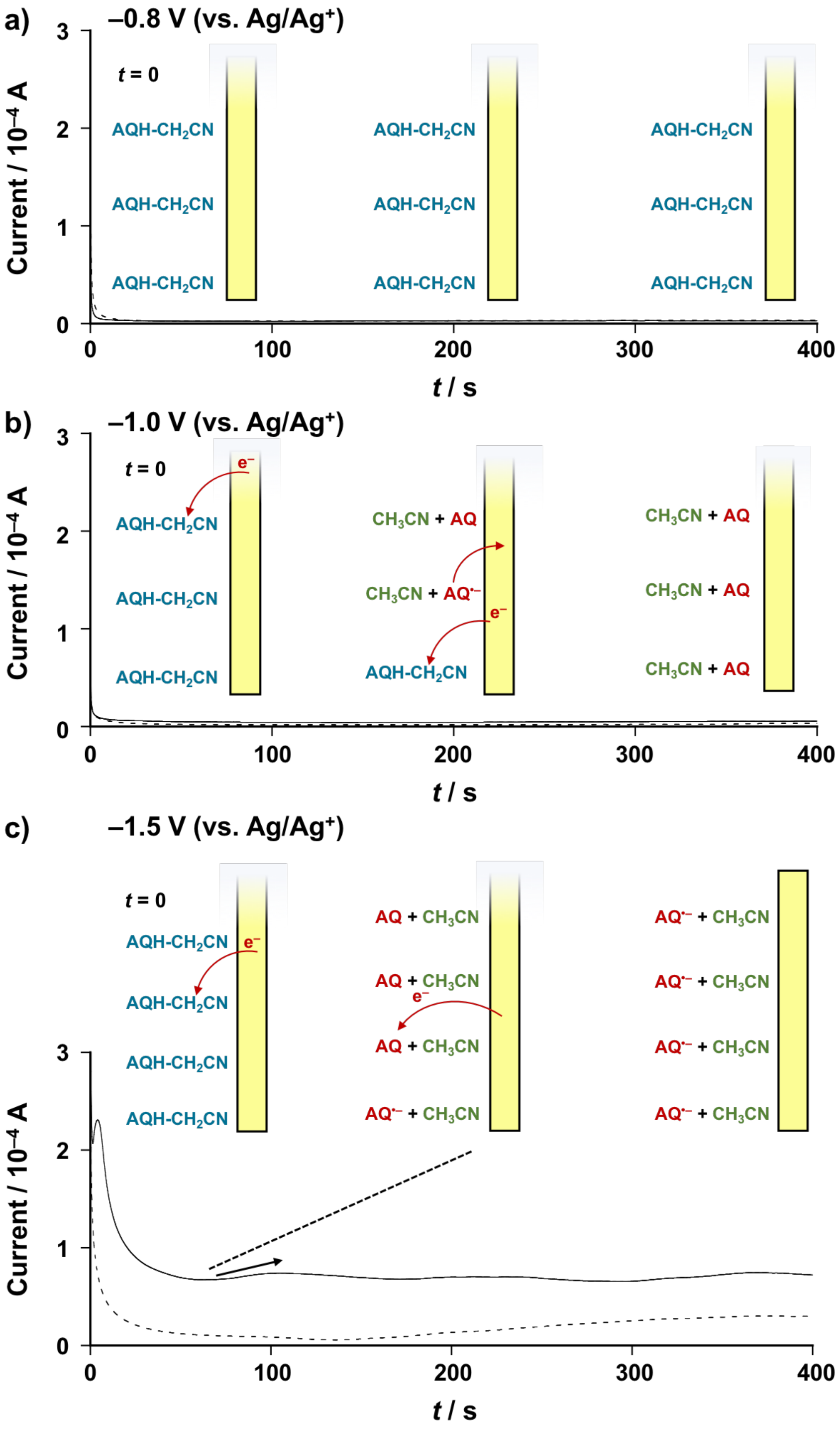

Figure S3. a-c) Time course of current change (solid lines) in AQH-CH$_2$CN (1.0×10^{-3} M) under applying a) −0.8 V, b) −1.0 V, and c) −1.5 V (vs. Ag/Ag$^+$) potential in deaerated acetonitrile containing 0.1 M TBAP. Dashed lines show the background current. Insets: Schematic representation of the reactions occurred around the surface of the working electrode at the corresponding time.

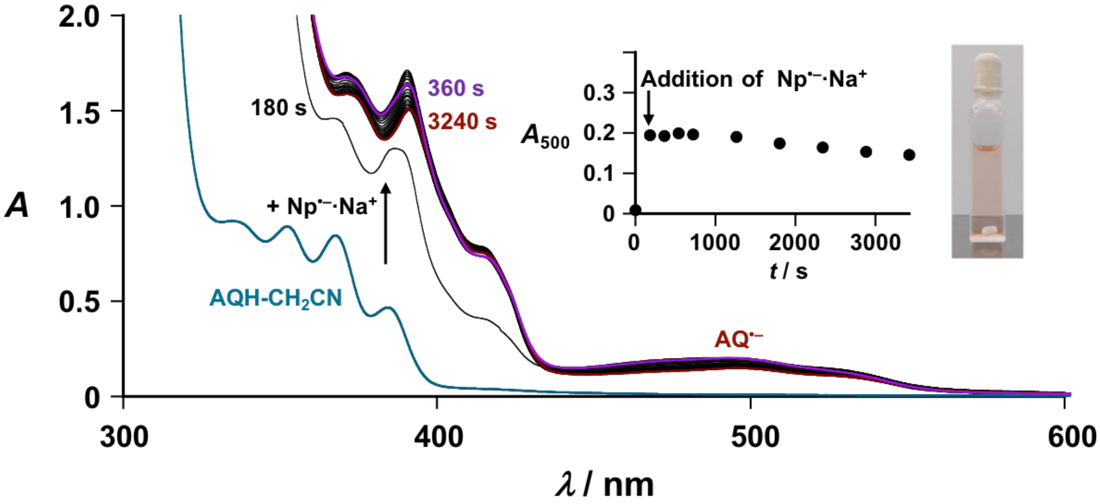

Figure S4. UV/Vis absorption spectra of AQH-CH₂CN (1.0×10^{-2} M) before (blue line) and after addition of $Np^{\bullet -}{\cdot}Na^+$ (1.0×10^{-3} M) in deaerated THF. Inset: Corresponding time course at absorbance at 500 nm and photograph after completing the reaction.

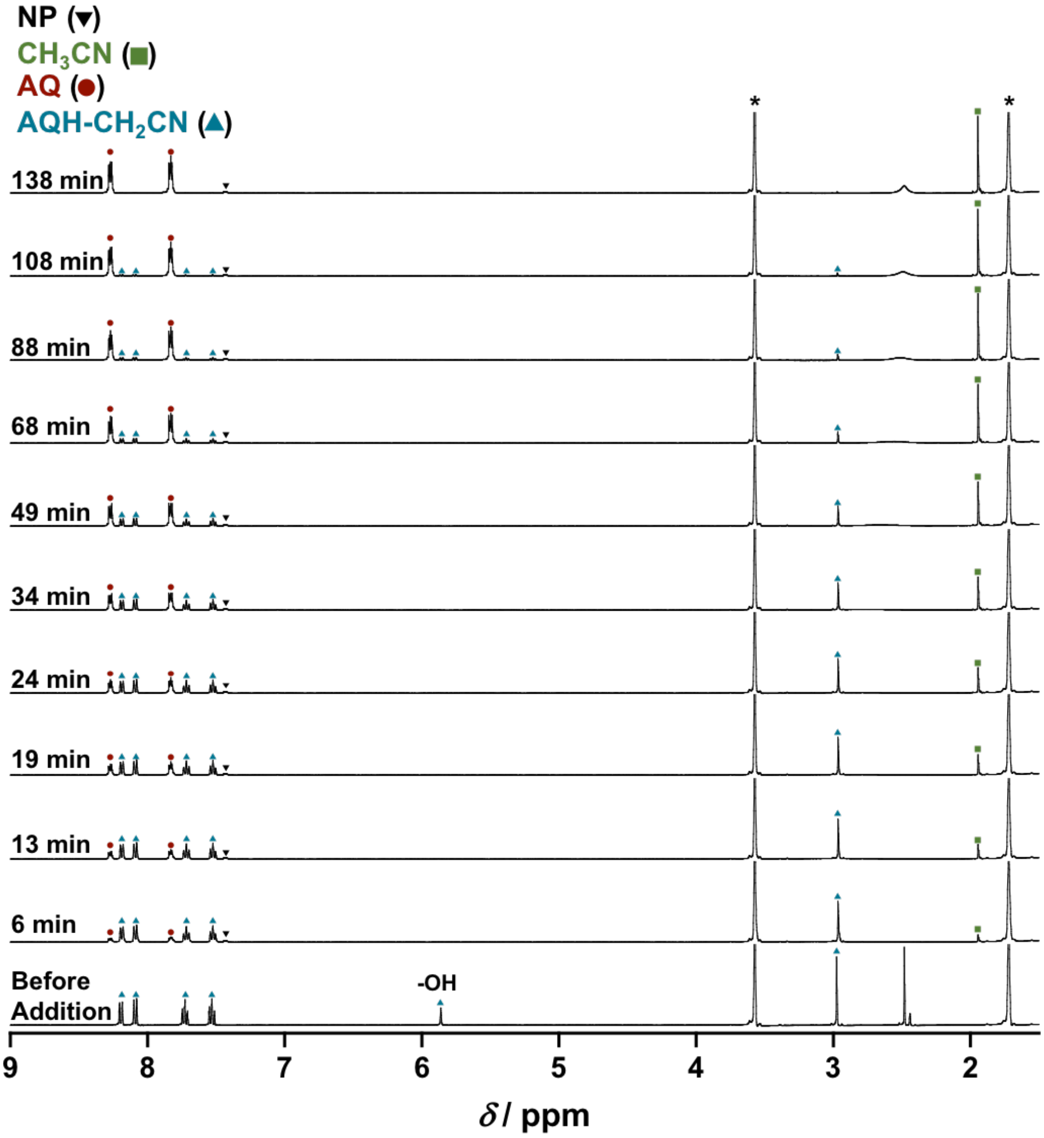

***Figure S5*.** Stacked ^{1}H NMR spectra of AQH-CH$_2$CN (2.0×10^{-2} M) upon addition of Np$^{\bullet-}\cdot$Na$^+$ (2.0×10^{-3} M) in THF-d_8. Signals annotated by asterisk is arising from the solvent.

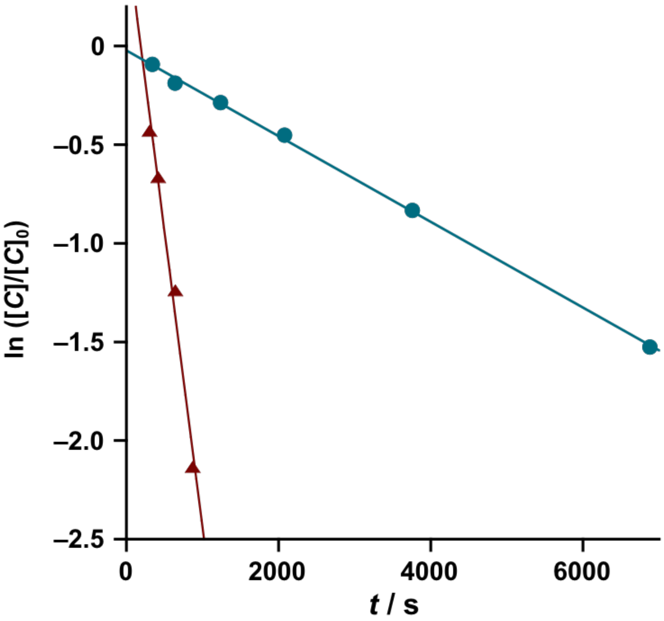

Figure S6. Plots of ln ($[C]/[C]_0$) versus t for the conversion of AQH-CH_2CN (2.0×10^{-2} M) to AQ by addition of $Np^{\bullet -}\cdot Na^+$ (blue circles: 5.0×10^{-4} M, red triangles: 1.5×10^{-3} M) in deaerated THF-d_8, where $[C]_0$ denotes the initial concentration of AQH-CH_2CN (2.0×10^{-2} M), and $[C]$ represents the concentration of AQH-CH_2CN during the reaction.

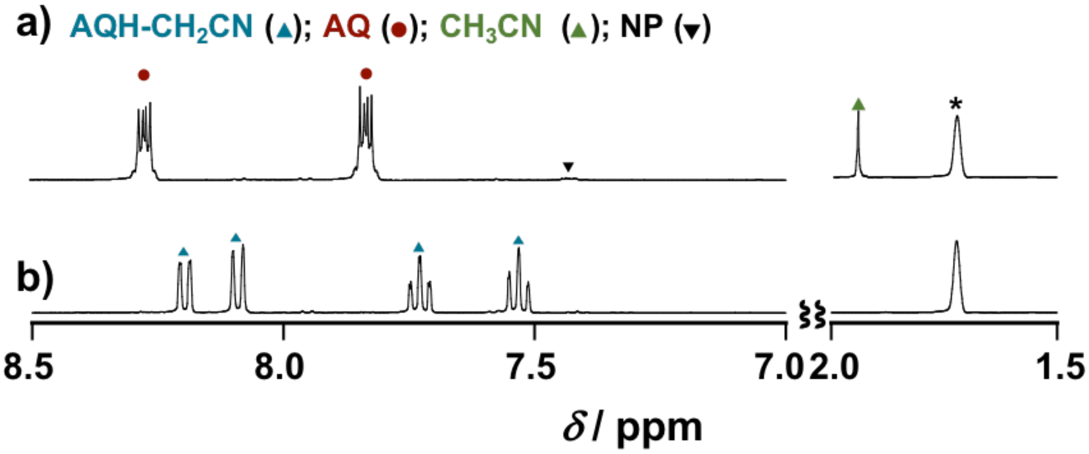

Figure S7. a,b) ^{1}H NMR spectra of AQH-CH_2CN (2.0×10^{-2} M) b) before addition, a) 1 day after addition of $Np^{\bullet -}\cdot Na^+$ (5.0×10^{-4} M) in deaerated THF-d_8. Signal annotated by asterisk is arising from the solvent. The intensity of spectra at 1.5–2.0 ppm is scaled vertically for clarity.

Binding Studies on CT Complexes (S8–S16, S21 and S22): Prior to perform the experiments, binding energy of U_HAnt_2 with AQ (oxidized form) and that with $AQ^{\bullet-}$ (reduced form) were predicted by DFT [DFT/CAM-B3LYP-6-31G(d), IEFPCM: THF]. The DFT studies indicate that binding of U_HAnt_2 with AQ (oxidized form) results in –2.99 kcal mol^{-1} stabilization (Figure S8), conversely binding between U_HAnt_2 with $AQ^{\bullet-}$ (reduced form) destabilizes the system +1.46 kcal mol^{-1} (Figure S8). AQ showed a reversible cyclic voltammogram even in the presence of U_HAnt_2 (Figure S21), suggesting that $AQ^{\bullet-}$ (reduced form) remains stable even in the presence of U_HAnt_2, therefore there is a lack of effective interaction between them. Similarly, the one-electron reduction potential of AQH-CH_2CN (reactant) was unchanged in the presence of U_HAnt_2 (Figure S22). Thus, U_HAnt_2 co-existed has no effect on the electrocatalytic conversion of AQH-CH_2CN to AQ.

Complex formation between U_HAnt_2 and AQ was indicated by ^1H NMR titration experiments, where addition of AQ (0–7.0 mM) into U_HAnt_2 (3.5 mM in $CDCl_3$) caused up-field shifts of aromatic protons (H^7, H^8, and H^9) of the anthracene tweezers of U_HAnt_2 (Figure S9-S13). The observed up-field shifts are consistent with the $AQ \subset U_HAnt_2$ showing a D–A–D-type CT complex, where anthracene rings are shielded by the central anthraquinone plane (Figure 6a). Conversely, chemical shifts for most of aromatic protons ($H^{2'}$, $H^{3'}$, $H^{4'}$, and $H^{5'}$) corresponding to the linker unit of U_HAnt_2 remained almost unchanged during the NMR titration (Figure S9-S13).

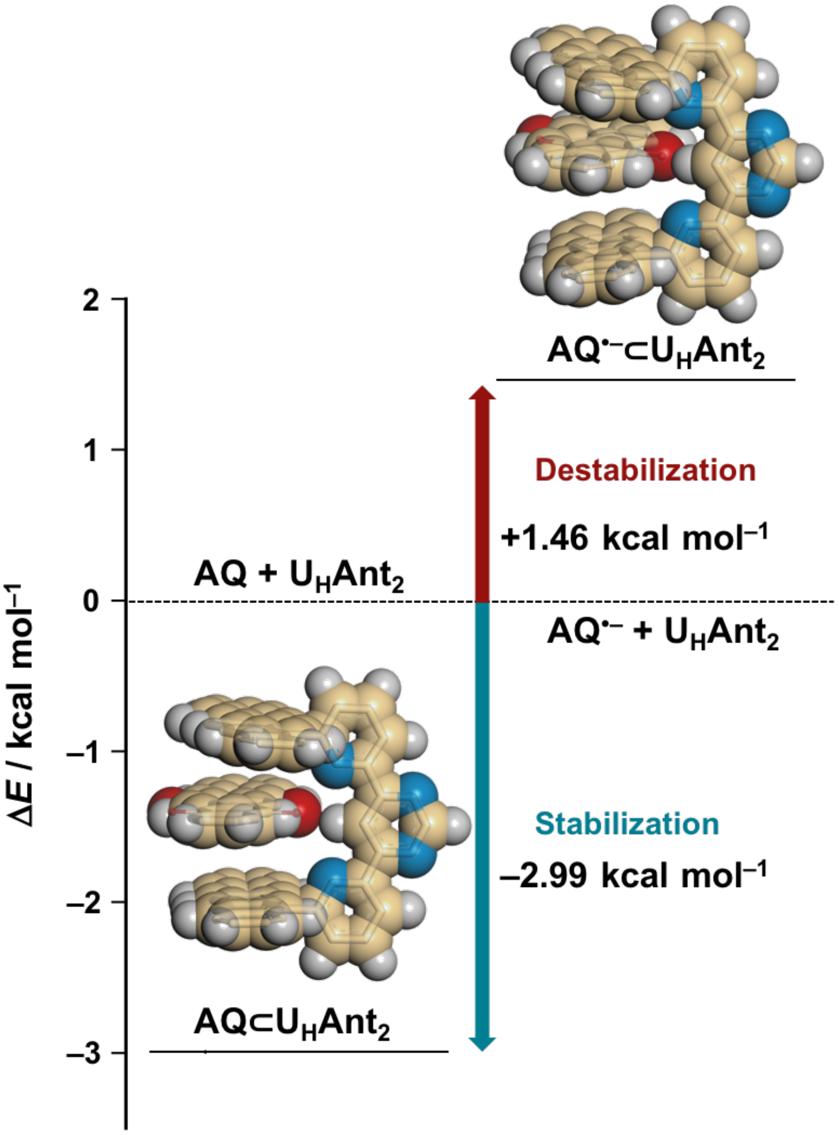

Figure S8. Binding energy [DFT/CAM-B3LYP-6-31G(d), IEFPCM: THF] between U$_H$Ant$_2$ and AQ, that between U$_H$Ant$_2$ and AQ$^{\bullet-}$ [DFT/CAM-UB3LYP-6-31G(d), IEFPCM: THF].

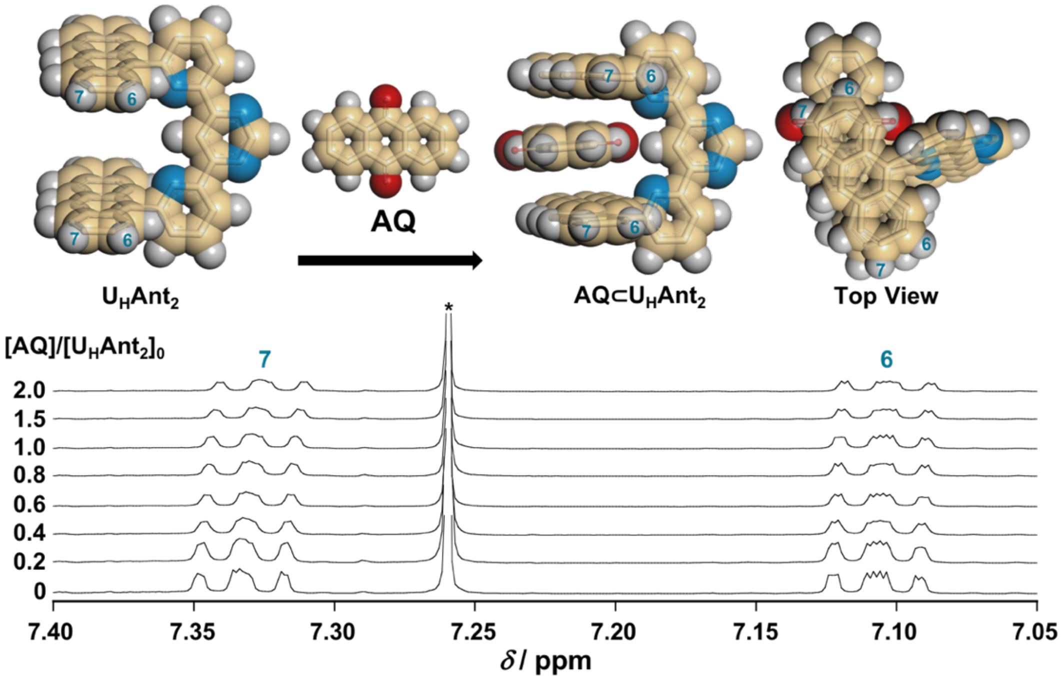

Figure S9**.** Stacked ^{1}H NMR spectra (for H^6 and H^7) of U_HAnt_2 (3.5×10^{-3} M) in the presence of AQ ($0–7.0 \times 10^{-3}$ M) in $CDCl_3$. Signal annotated by asterisk is arising from the solvent.

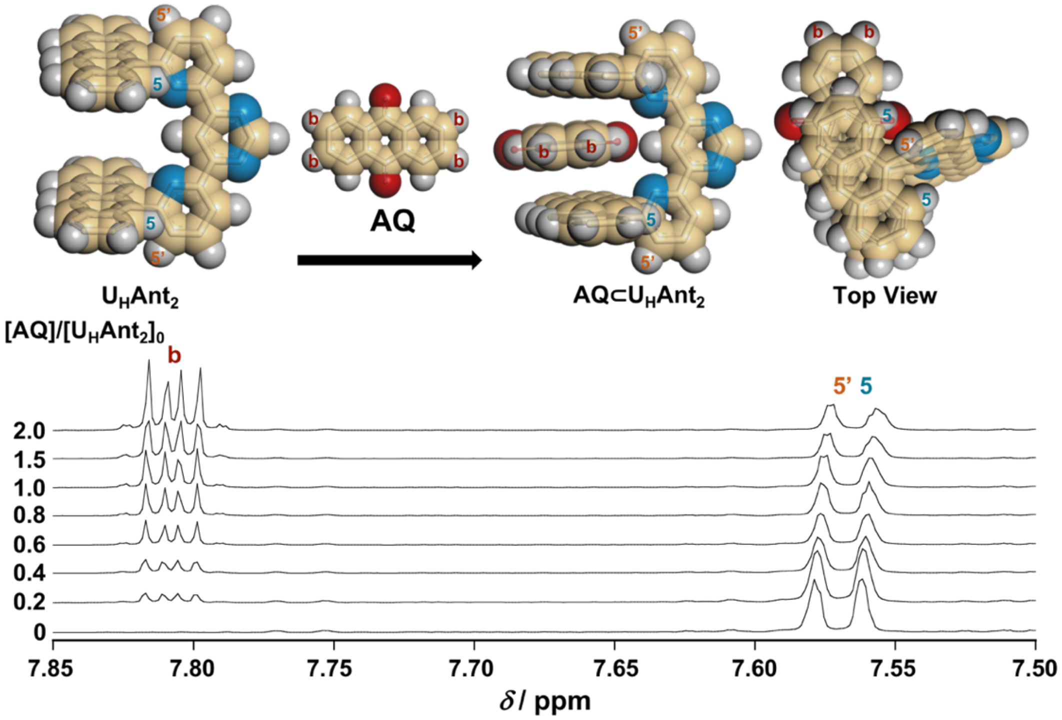

Figure S10**.** Stacked ^{1}H NMR spectra (for H^5, $H^{5'}$ and H^b) of U_HAnt_2 (3.5×10^{-3} M) in the presence of AQ ($0–7.0 \times 10^{-3}$ M) in $CDCl_3$.

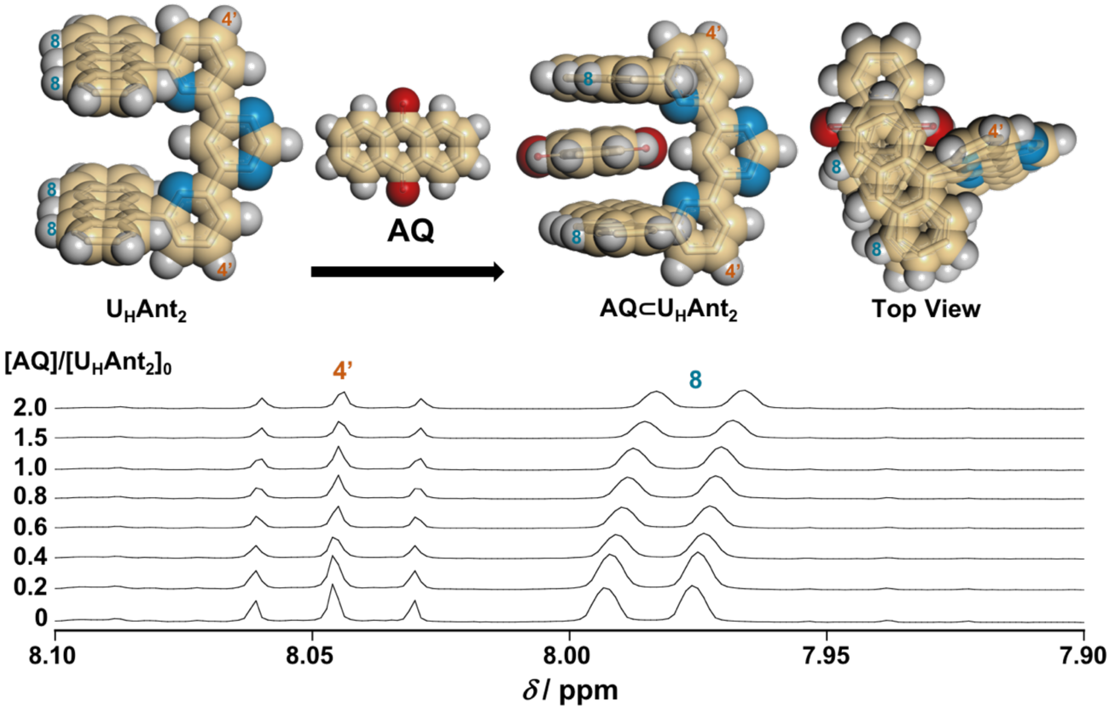

Figure S11. Stacked ^{1}H NMR spectra (for H$^{4'}$ and H^8) of U$_H$Ant$_2$ (3.5 × 10^{-3} M) in the presence of AQ (0–7.0 × 10^{-3} M) in CDCl$_3$.

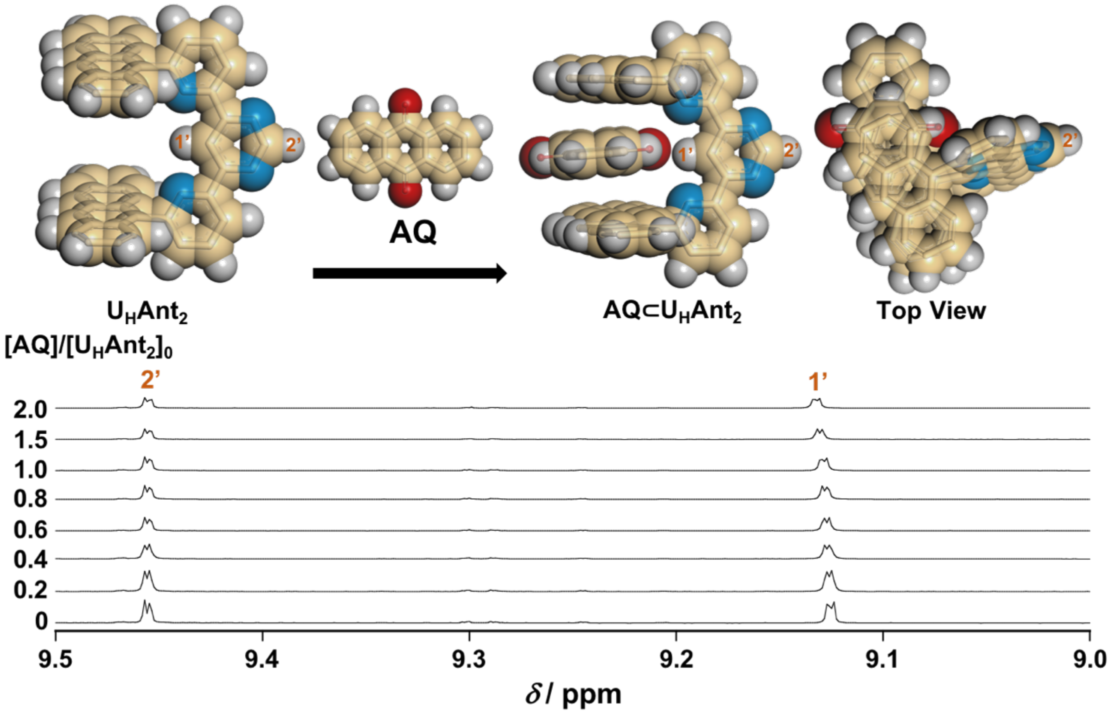

Figure S12. Stacked ^{1}H NMR spectra (for H$^{2'}$ and H$^{1'}$) of U$_H$Ant$_2$ (3.5 × 10^{-3} M) in the presence of AQ (0–7.0 × 10^{-3} M) in CDCl$_3$.

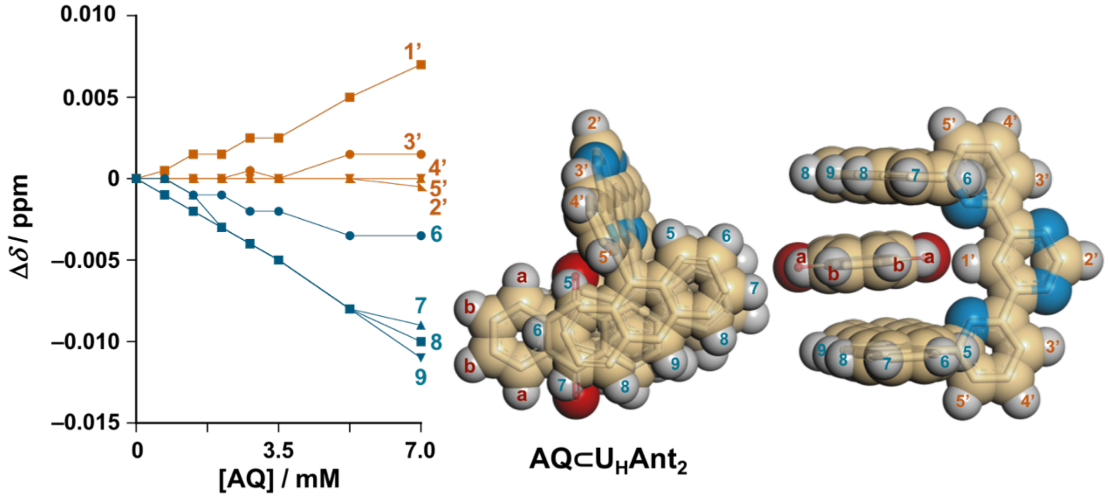

Figure S13. Plots of chemical shift changes of U_HAnt_2 versus concentration of AQ for NMR titration of U_HAnt_2 (3.5×10^{-3} M) by AQ ($0–7.0 \times 10^{-3}$ M) in $CDCl_3$.

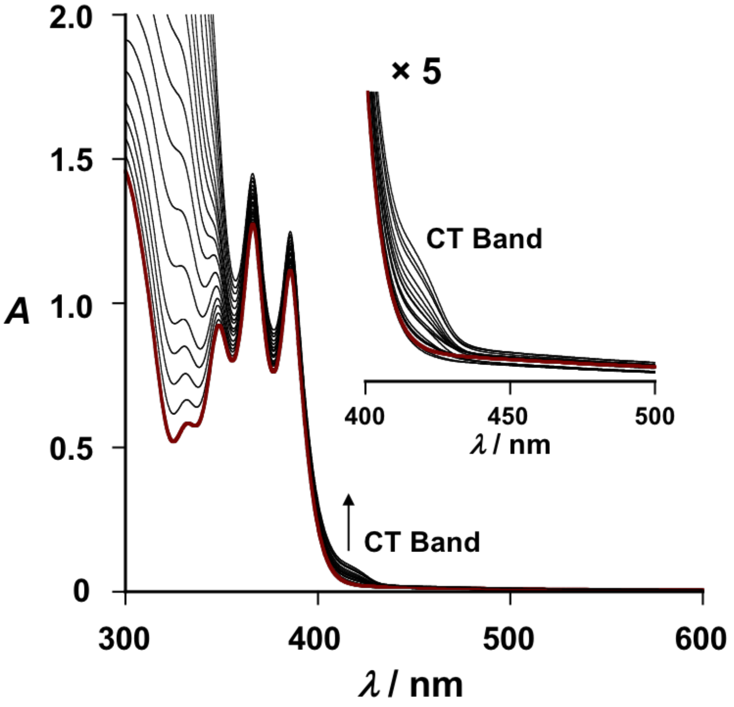

Figure S14. UV/Vis absorption spectra of U_HAnt_2 (8.0×10^{-4} M) in the presence of AQ [0 (red line)– 8.0×10^{-3} M] in THF containing 0.1 M TBAP (1 mm cuvette). Inset shows the vertically expanded spectra in the region of λ = 400–500 nm.

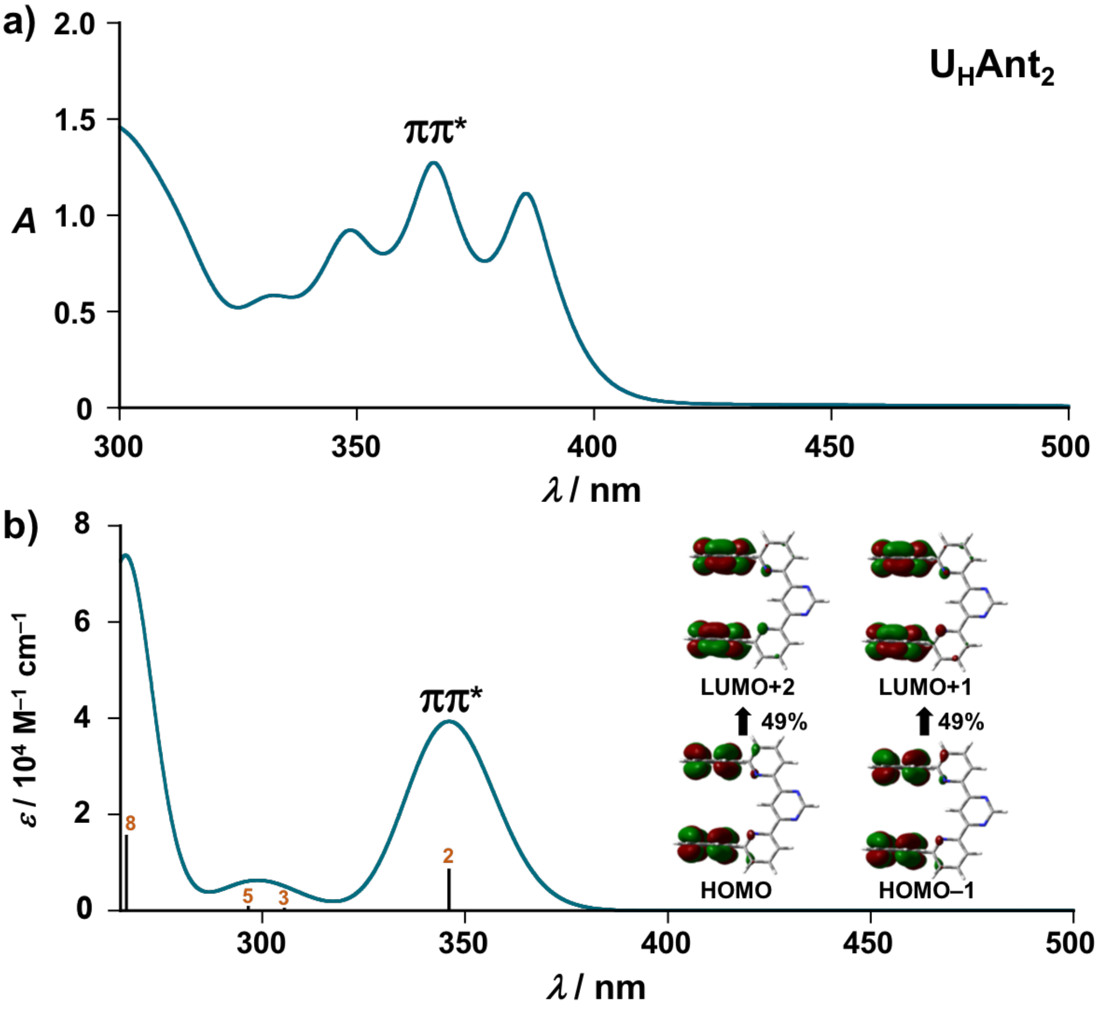

Figure S15. a) UV/Vis absorption spectra of U$_H$Ant$_2$ (8.0×10^{-4} M) in THF containing 0.1 M TBAP (1 mm cuvette). b) Calculated UV/Vis absorption spectrum [TD-DFT/CAM-B3LYP-6-31G(d), IEFPCM: THF] of the optimized structure of U$_H$Ant$_2$ [DFT/CAM-B3LYP-6-31G(d), IEFPCM: THF]. Inset: (b) Summary of excited state 2.

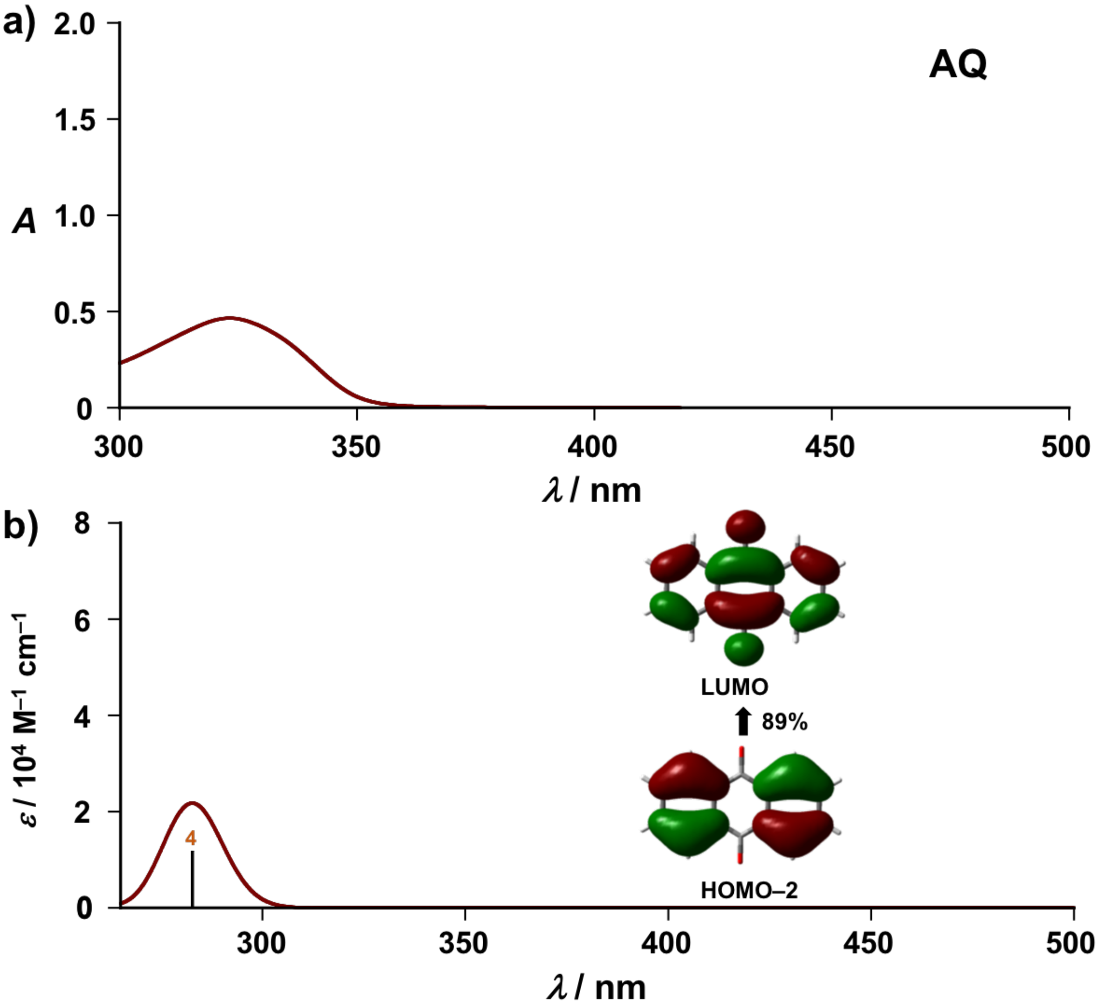

Figure S16. (a) UV/Vis absorption spectra of AQ (1.0×10^{-3} M) in THF containing 0.1 M TBAP (1 mm cuvette). (b) Calculated UV/Vis absorption spectrum [TD-DFT/CAM-B3LYP-6-31G(d), IEFPCM: THF] of the optimized structure of AQ [DFT/CAM-B3LYP-6-31G(d), IEFPCM: THF]. Inset: (b) Summary of excited state 4.

Assignment of CT Bands: Further assignment of CT band was performed with quinones having different one-electron reduction potentials, AQ (E^0_{red} = −1.35 V (vs. Ag/Ag$^+$)), 1,4-Naphthoquinone [NQ (E^0_{red} = −1.04 V (vs. Ag/Ag$^+$)], and 1,4-benzoquinone [Q (E^0_{red} = −0.86 V (vs. Ag/Ag$^+$)]. The DFT calculations [DFT/CAM-B3LYP-6-31G(d), IEFPCM: $CHCl_3$] indicate that bindings of U_HAnt_2 with the quinones result in –3.20–3.62 kcal mol^{-1} stabilization (Figure S17), which underlines that CT complex formation of U_HAnt_2 with the quinones is convincing. The CT complex formations for $NQ\subset U_HAnt_2$ and $Q\subset U_HAnt_2$ were also confirmed by ^{1}H NMR titration experiments as employed for $AQ\subset U_HAnt_2$ (Figure S18 and S19). The $AQ\subset U_HAnt_2$, $NQ\subset U_HAnt_2$, and $Q\subset U_HAnt_2$ exhibited the CT bands at longer wavelength region, in which their

CT absorption maxima show red shift (Figure S20a-c) with increasing the oxidizing power of the quinones (AQ → NQ → Q). Calculated UV/Vis absorption spectra obtained with TD-DFT [CAM-B3LYP-6-31G(d), IEFPCM: $CHCl_3$] using the optimized structures of AQ⊂$U_H$$Ant_2$, NQ⊂$U_H$$Ant_2$, and Q⊂$U_H$$Ant_2$ successfully reproduced the observed trend (Figure S20d-f).

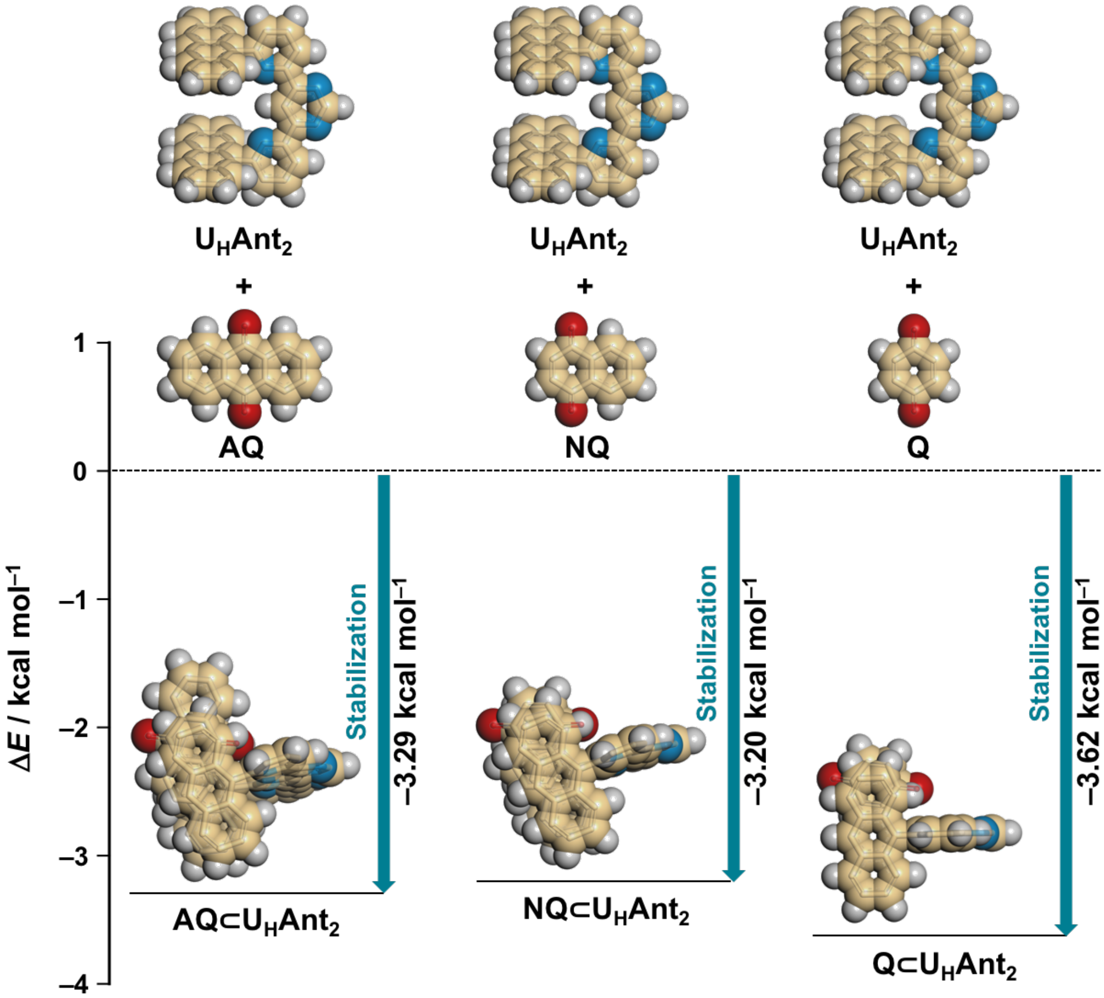

Figure S17. Binding energy [DFT/CAM-B3LYP-6-31G(d), IEFPCM: $CHCl_3$] of $U_H$$Ant_2$ with AQ, NQ, and Q.

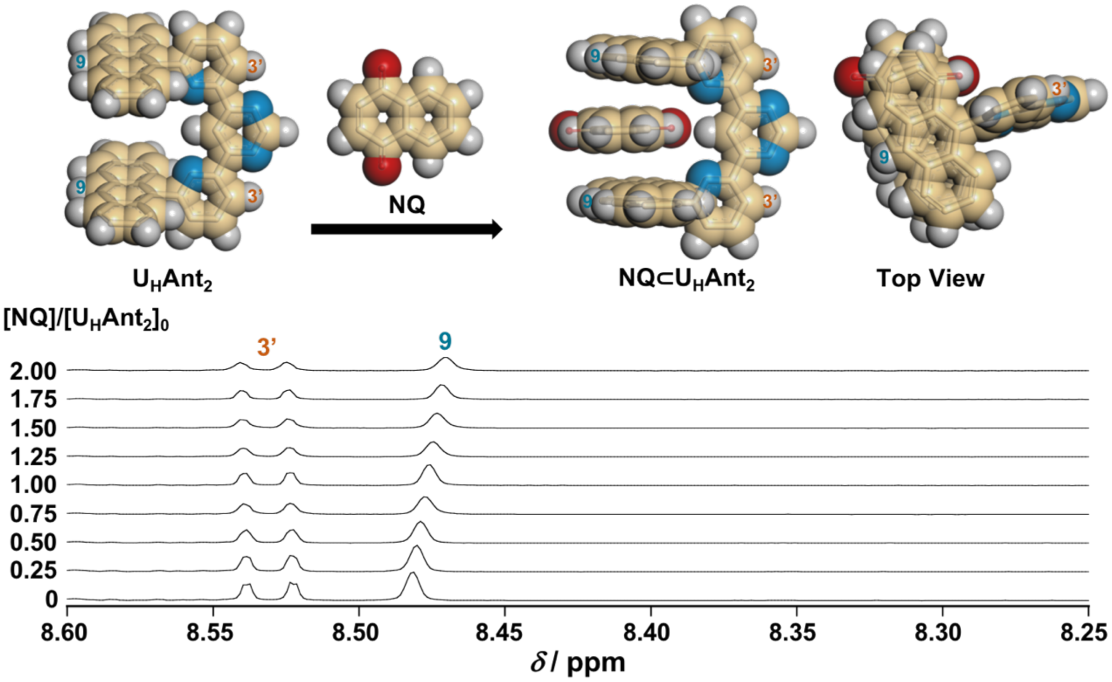

Figure S18. Stacked ^{1}H NMR spectra (for $H^{3'}$ and H^9) of U$_H$Ant$_2$ (3.5×10^{-3} M) in the presence of NQ ($0–7.0 \times 10^{-3}$ M) in CDCl$_3$.

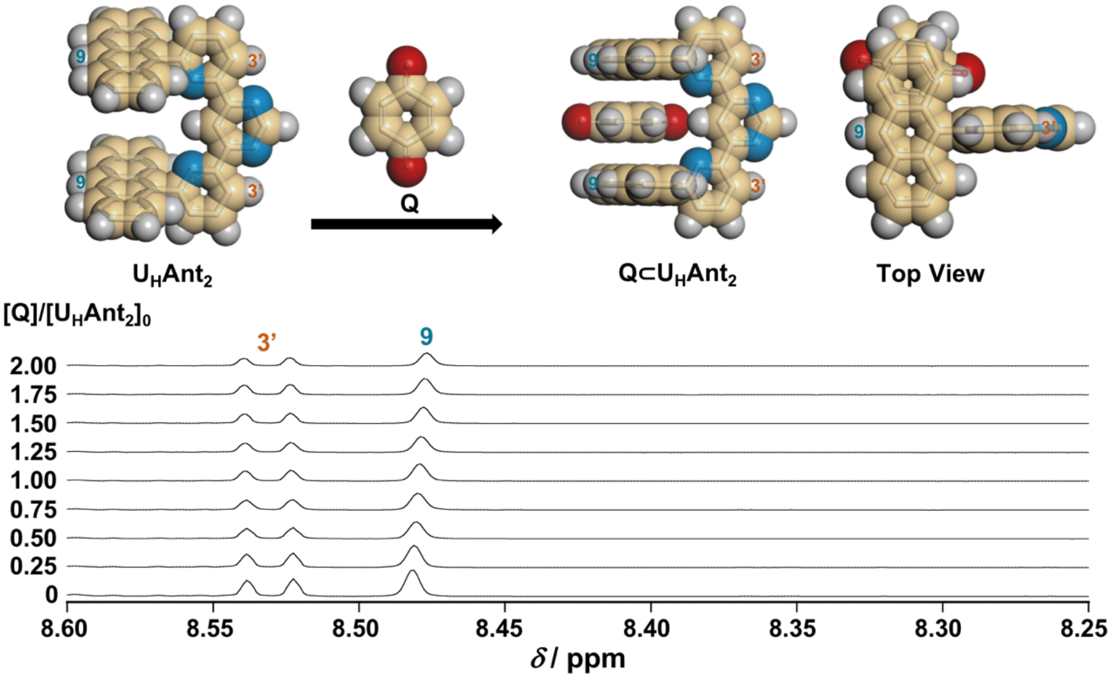

Figure S19. Stacked ^{1}H NMR spectra (for $H^{3'}$ and H^9) of U$_H$Ant$_2$ (3.5×10^{-3} M) in the presence of Q ($0–7.0 \times 10^{-3}$ M) in CDCl$_3$.

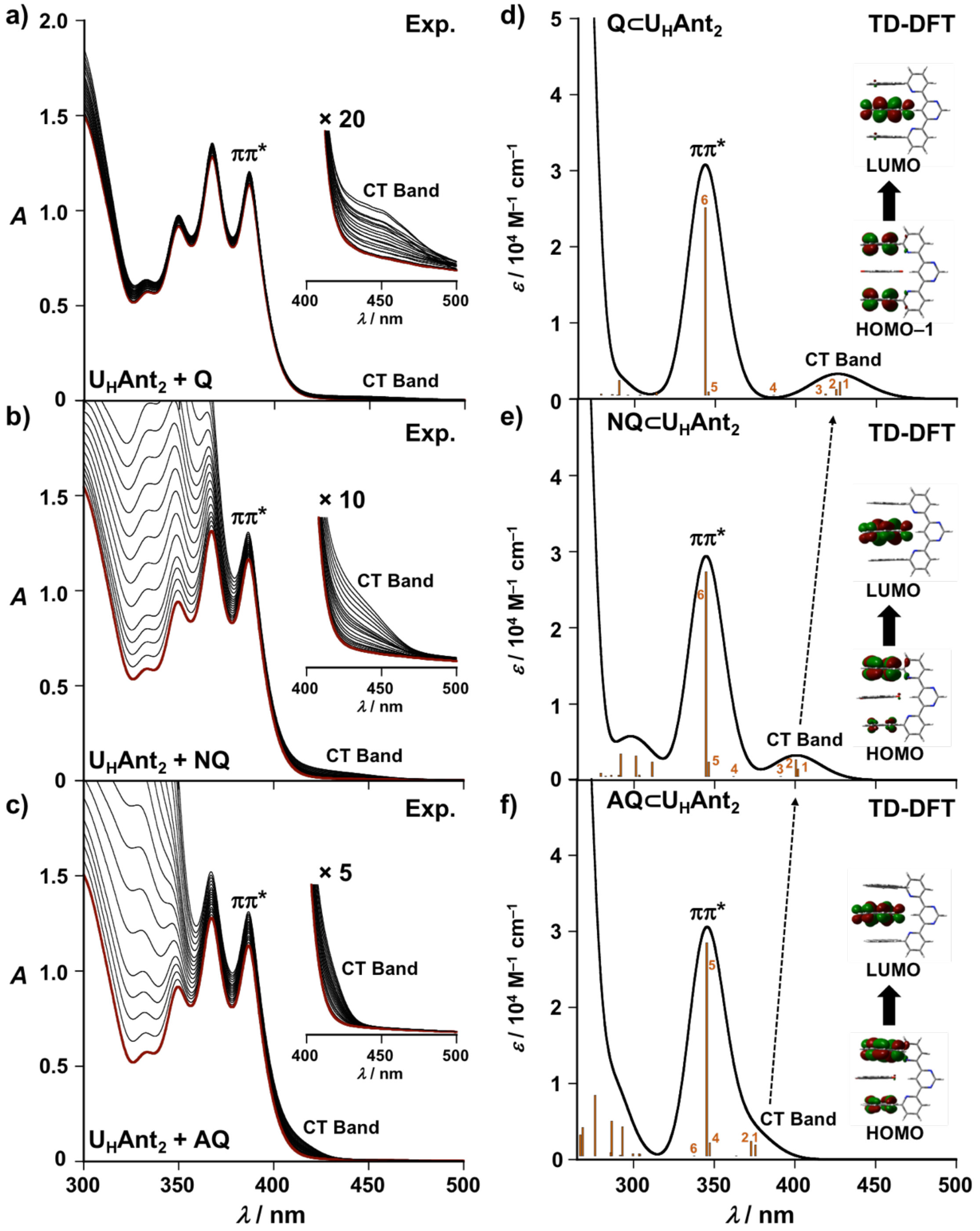

Figure S20. (a-c) UV/Vis absorption spectra of $\mathrm{U_HAnt_2}$ (8.0 × 10^{-4} M) in the presence of (a) Q, (b) NQ, and (c) AQ [concentrations: 0 (red line)– 8.0 × 10^{-3} M] in $\mathrm{CHCl_3}$ (1 mm cuvette). Insets show the vertically expanded spectra in the region of λ = 400–500 nm. (d-f) Calculated UV/Vis absorption spectra [TD-DFT/CAM-B3LYP-6-31G(d), IEFPCM: $\mathrm{CHCl_3}$] of the optimized structure of (d) Q⊂$\mathrm{U_HAnt_2}$, (e) NQ⊂$\mathrm{U_HAnt_2}$, and (f) AQ⊂$\mathrm{U_HAnt_2}$ [DFT/CAM-B3LYP-6-31G(d), IEFPCM: $\mathrm{CHCl_3}$]. Insets show the dominant contribution on excited state 1.

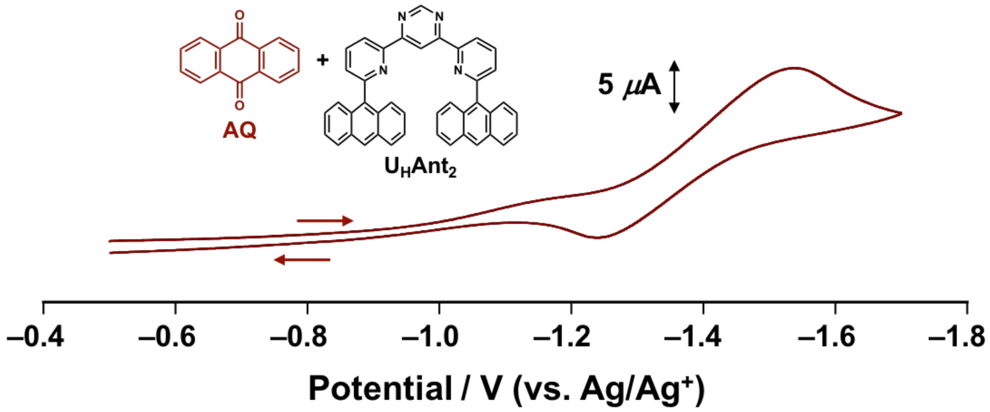

Figure S21. Cyclic voltammogram of AQ (8.0×10^{-4} M) in the presence of U_HAnt_2 (8.0×10^{-4} M) in deaerated THF containing 0.1 M TBAP. Scan rate is 200 mV/s.

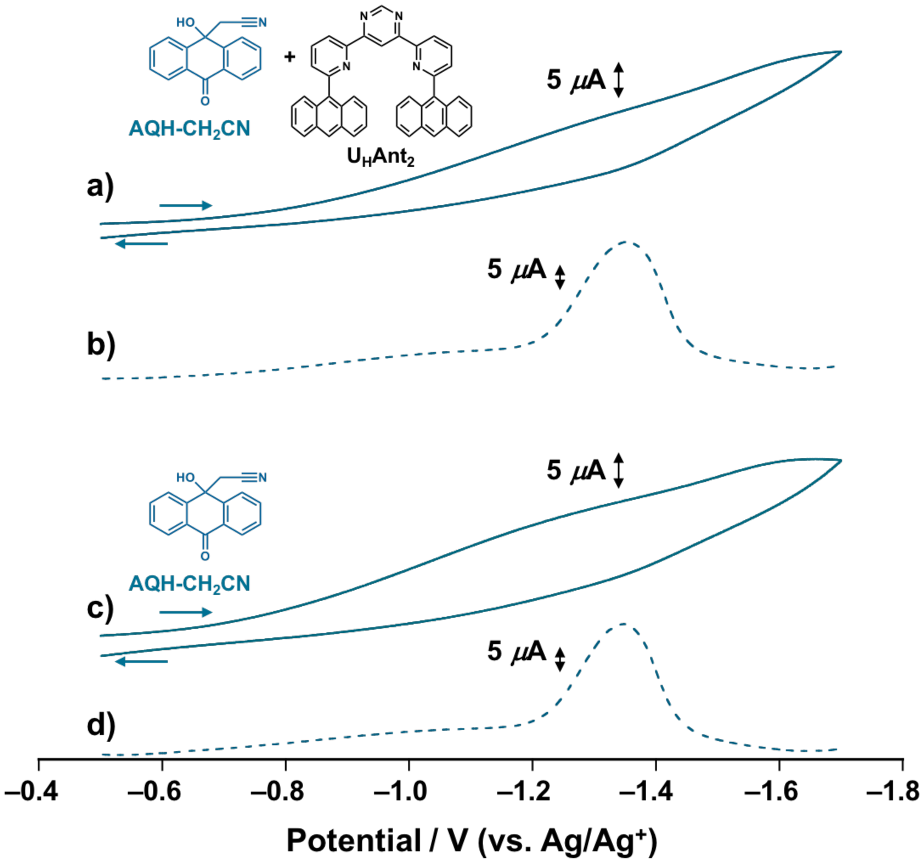

Figure S22. (a,c) Cyclic voltammogram and (b,d) differential pulse voltammetry of (a,b) AQH-CH$_2$CN (8.0×10^{-4} M) in the presence of U_HAnt_2 (8.0×10^{-4} M) and (c,d) AQH-CH$_2$CN (8.0×10^{-4} M) in deaerated THF containing 0.1 M TBAP. Scan rate is 200 mV/s.

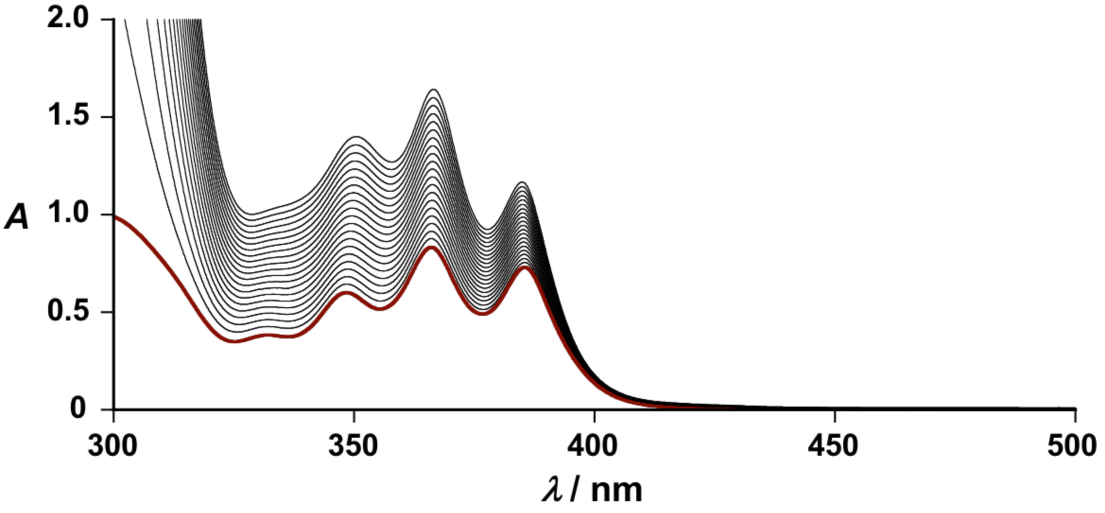

Figure S23. UV/Vis absorption spectra of U_HAnt_2 (5.0×10^{-5} M) in the presence of AQH-CH_2CN [0 (red line)– 1.0×10^{-2} M] in THF.

Chemical Reduction Turns-On CT Complex Formation (S24): We also performed electrocatalytic conversion of AQH-CH_2CN to AQ initiated by chemical reduction using 0.1 equiv of $Np^{\bullet-}\cdot Na^+$ in the presence of U_HAnt_2 (Figure S24). As in the case of the electrocatalytic conversion initiated by the electrochemical reduction, conversion of AQH-CH_2CN into AQ was

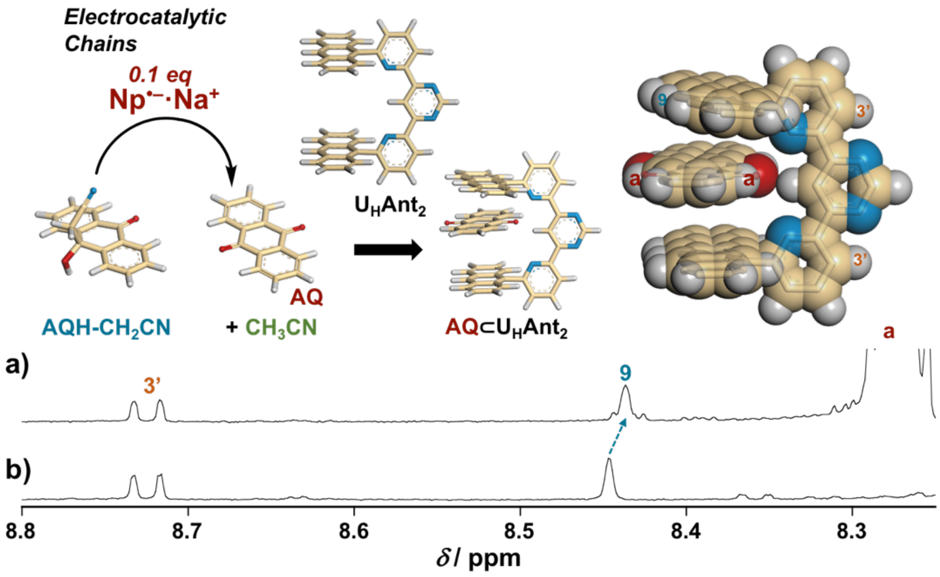

Figure S24. ^1H NMR spectra (for $H^{3'}$ and H^9) of AQH-CH_2CN (2.0×10^{-2} M) (a) after and (b) before addition of $Np^{\bullet-}\cdot Na^+$ (2.0×10^{-3} M) in the presence of U_HAnt_2 (8.0×10^{-4} M) in THF-d_8.

successfully achieved, whereas no degradation of U$_H$Ant$_2$ was observed (Figure S24). After the conversion of AQH-CH$_2$CN into AQ, the appreciable up-field shifts of anthracene aromatic protons corresponding to the anthracene tweezers of U$_H$Ant$_2$ was also observed (Figure S24), which is specific to the event for the insertion of AQ into U$_H$Ant$_2$ to generate the CT complex AQ⊂U$_H$Ant$_2$ (Figure 6b). Thus, electrocatalytic conversion of AQH-CH$_2$CN to AQ initiated by chemical reduction was also capable of turning on the CT complex formation. As far as we examined, no appreciable macroscopic change can be found in the catalytic formation of the CT complex.

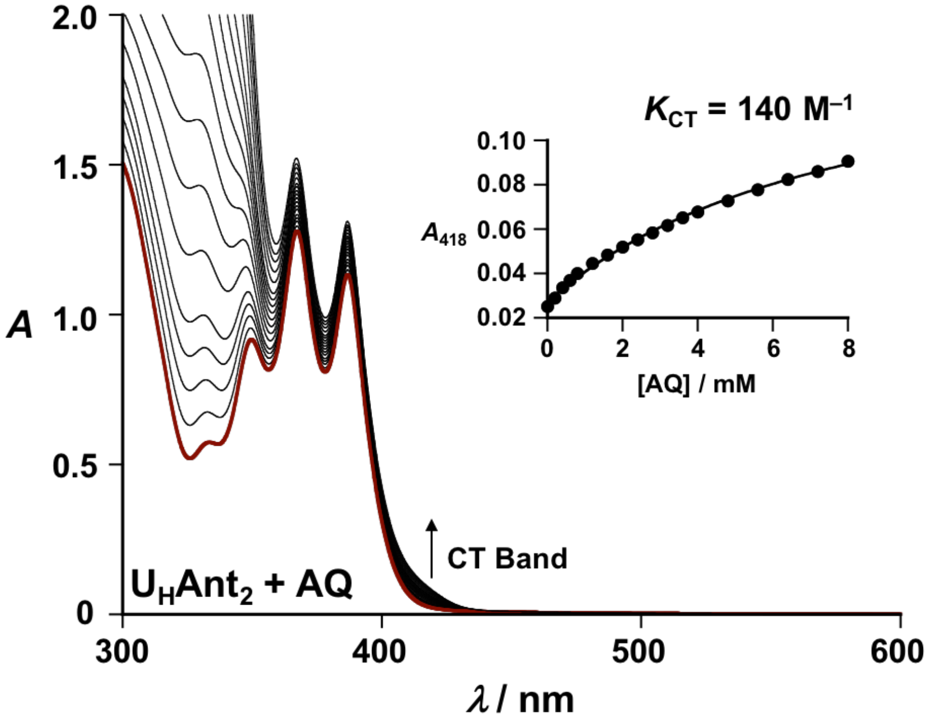

Figure S25. UV/Vis absorption spectra of U$_H$Ant$_2$ (8.0×10^{-4} M) in the presence of AQ [0 (red line)– 8.0×10^{-3} M] in CHCl$_3$ (1 mm cuvette). Inset shows plot of absorbance at 418 nm versus [AQ].

References

1 A. Petitjean, R. G. Khoury, N. Kyritsakas and J.-M. Lehn, *J. Am. Chem. Soc.*, 2004, **126**, 6637–6647.

2 K. Saito, M. Ohtani and S. Fukuzumi, *J. Am. Chem. Soc.*, 2006, **128**, 14216–14217.

3 S. Fukuzumi, T. Suenobu, T. Hirasaka, R. Arakawa and K. M. Kadish, *J. Am. Chem. Soc*. 1998, **120**, 9220–9227.